# Numerical investigation of the noise generation of electric motors in urban air mobility vehicles<sup>a)</sup> FREE

Sebastian Hakansson; Philipp Schulze; Ralf Burgmayer; Erik W. Schneehagen; Thomas F. Geyer



J. Acoust. Soc. Am. 158, 2647-2658 (2025)

https://doi.org/10.1121/10.0039427





# Articles You May Be Interested In

Psychoacoustic evaluation of different fan designs for an urban air mobility vehicle with distributed propulsion system

J. Acoust. Soc. Am. (March 2025)

Modification of Amiet's model for turbulence-ingestion noise prediction in rotors

J. Acoust. Soc. Am. (July 2025)

Manipulation of surface pressure fluctuations for a tandem symmetric airfoil configuration using the trailingedge treatments

Physics of Fluids (July 2025)











# Numerical investigation of the noise generation of electric motors in urban air mobility vehicles<sup>a)</sup>

Sebastian Hakansson, Philipp Schulze, Ralf Burgmayer, Erik W. Schneehagen, and Thomas F. Geyer<sup>b)</sup> *Institute of Electrified Aero Engines, Environmental Impact and Sensor Technology Department, German Aerospace Center (DLR), Cottbus 03046, Germany* 

#### **ABSTRACT:**

Current concepts of urban air mobility vehicles usually rely on a set of individual electrically driven propulsion systems. Although aerodynamically generated noise from the rotors or fans remains the main contribution to the overall noise, noise generated by electric machines may well add to the total noise. This is especially true for fast-spinning electric motors that cause high-frequency noise contributions, which may notably increase the total noise and lead to unwanted psychoacoustic effects. In the current paper, the noise generation of two versions of permanent magnet synchronous machines in a conventional inrunner configuration, intended for use in a concept vehicle propelled by eight tiltable rotors, is investigated through numerical simulations and analytical models. One version is a direct drive, designed to deliver the torque and rotational speed required for the rotor directly. The other is a geared version, delivering a higher rotational speed and lower torque, thus requiring an additional gear box to drive the rotor. The results show that the geared motor version leads to notable noise contributions at frequencies of 2 kHz and 9 kHz. Coupled with a high radiation efficiency in this frequency range, the findings imply that noise from electric machines contributes to the total noise from the vehicle. © 2025 Acoustical Society of America. https://doi.org/10.1121/10.0039427

(Received 6 May 2025; revised 5 September 2025; accepted 9 September 2025; published online 1 October 2025)

[Editor: Damiano Casalino] Pages: 2647–2658

# **NOMENCLATURE**

- 2p Number of poles p
- A Stator outer surface  $(m^2)$
- $B_{\rm g}$  Magnetic flux density in the air gap of the permanent magnets (T)
- $B_{\rm rad}$  Magnetic flux density in the radial direction (T)
- $B_{tan}$  Magnetic flux density in the tangential direction (T)
- $b_{14}$  Slot opening (m)
- $b_{\phi}$  Coefficient of the Fourier series higher space harmonics
- $c_0$  Speed of sound (m/s)
- $c_{\rm L}$  Longitudinal wave velocity (m/s)
- $D_{1in}$  Inner (bore) diameter of the stator (m)
- $D_{1out}$  Outer diameter of the stator (m)
- $D_{2in}$  Inner diameter of the rotor (m)
  - d<sub>m</sub> Radial vibration displacement (m)
  - E Young's modulus (Pa)
  - F Force acting on the stator teeth m(N)
  - $F_{\rm m}$  Force amplitude of mode m (N)
  - f Frequency (Hz)
  - f<sub>e</sub> Electrical frequency (Hz)
- $f_{\text{nm}}$  Eigenfrequencies of modes, longitudinal modes n and circumferential modes m (Hz)
  - $f_r$  Frequency of the force component of order r (Hz)

- $f_{\rm ring}$  Ring frequency (Hz)
  - g Air gap height (m)
  - h Wall thickness of cylindrical shell (m)
- h<sub>m</sub> Magnet thickness (m)
- $h_{\rm sl}$  Magnification factor (m)
- J Root mean square (rms) current density (A/mm<sup>2</sup>)
- $k_0$  Acoustic wave number (m<sup>-1</sup>)
- $k_{0k}$  Stator slot opening coefficient
- $k_{\rm a}$  Axial wave number (m<sup>-1</sup>)
- k<sub>c</sub> Carter coefficient
- $k_{\rm ep}$  Wave number of the equivalent plate (m<sup>-1</sup>)
- $k_{\rm r}$  Wave number in radial direction (m<sup>-1</sup>)
- $k_{s\phi}$  Rotor permanent magnet skew factor
- $k_{\rm sk}$  Stator slot skew factor
- $k_x$  Wave number of the equivalent plate in x direction  $(m^{-1})$
- $k_y$  Wave number of the equivalent plate in y direction  $(m^{-1})$
- $L_{\rm w}$  Sound power level (dB)
  - l Lamination length of the stator (m)
- $l_{arc}$  Length of the arc force acts on (m)
- $M_{\rm c}$  Mass of the cylindrical shell (kg)
- $M_{\rm s}$  Mass of the stator (kg)
  - *m* Circumferential mode number
- $m_{\rm ph}$  Number of phases
- Number of stator slots
- $N_{\rm r}$  Rated (rotational) speed (min<sup>-1</sup>)
- n Longitudinal mode number
- P (Peak) power (W)

a)This paper is part of a special issue on Advanced Air Mobility Noise: Predictions, Measurements, and Perception.

b)Email: thomas.geyer@dlr.de



 $P_{\text{ERP}}$  Equivalent radiated power (W)

 $p_{\text{mag}}$  Force density (N/m<sup>2</sup>)

 $P_{\rm mr}$  Magnetic force component of circumferential order m and spatial order r  $(N/m^2)$ 

 $p_r$  Spatial distribution of the magnetic pressure (force density at space order r)  $(N/m^2)$ 

 $p_{\rm rad}$  Force density in radial direction (N/m<sup>2</sup>)

 $p_{tan}$  Force density in tangential direction (N/m<sup>2</sup>)

q Number of slots per phase per pole

r Space order

r<sub>c</sub> Center radius of cylindrical shell (m)

 $r_{\rm o}$  Outer radius of cylindrical shell (m)

T Torque (Nm)

t Time (s)

 $t_1$  Stator slot pitch (m)

V DC bus voltage (V)

 $v_{\rm m}$  Vibration velocity of mode m (m/s)

 $v_{\rm n}$  Normal surface vibration velocity (m/s)

 $v_{\rm nm}$  Vibration velocity for the modes n and m (m/s)

x Linear circumferential coordinate (m)

α Electrical angle (°)

γ Constant depending on slot opening and air gap

 $\kappa_m$   $\;\;$  Coefficient accounting for the added mass of the stator teeth

 $\lambda_z$  Longitudinal wave length (m)

 $\mu$  Number of higher space harmonics

 $\mu_0$  Magnetic permeability of free space (H/m)

 $\nu$  Poisson's ratio

 $\rho_0$  Fluid density (kg/m<sup>3</sup>)

 $\rho_m$  Density of stator lamination (kg/m<sup>3</sup>)

 $\sigma$  Radiation efficiency

 $\tau$  Pole pitch (m)

 $\phi$  Harmonics of space mode r

ω Acoustic circular frequency (Hz)

 $\omega_{\rm m}$  Circular frequency of mode m (Hz)

 $\omega_r$  Circular frequency of spatial mode r (Hz)

#### I. INTRODUCTION

The concept of urban air mobility (UAM) as a means of transport especially in densely populated urban areas is receiving increased attention in various fields of research (see, for example, studies by Straubinger *et al.*, Brown and Harris, and Johnson and Silva with many potential vehicle designs being discussed and several of them already in advanced design or test stages. These vehicles can be designed to satisfy specific use cases and missions and, hence, differ in size, shape, and mass as well as in the selected propulsion system, which could be open rotors or ducted fans.

However, one main concern of UAM is the noise generated by the propulsion system, <sup>6</sup> especially as most concepts feature several propulsors, which may lead to additional unwanted effects such as acoustic interference, modulation, and interaction. Many existing studies rely on numerical or analytical approaches to evaluate the noise from UAM vehicles, as experimental data are not yet available.

In the introductory study by Little et al., the use of fundamental acoustic metrics for the noise prediction of UAM vehicles is discussed, with the aim of paving the way for the early aeroacoustic design of such vehicles in order to meet noise regulations. The feasibility of a chosen set of metrics is then demonstrated using numerical simulations for characteristic cases like a vehicle with just one isolated propeller and one with multiple in-phase propellers. In a companion study, 8 the authors present a prediction model for the conceptual design and preliminary aeroacoustic and aerodynamic analysis of UAM vehicles. In the recent numerical study by Ko et al.,9 the effect of speed and trajectory on the landing noise of UAM vehicles is analyzed using a comprehensive noise prediction framework. The noise source strength during landing was found to be affected by operational parameters of the rotors, such as rpm trim conditions; by wake dynamics of the propellers; as well as by rotorwake interactions.

Due to the fact that UAM vehicles are driven by several propulsors, which can lead to effects like interference, modulation, and interaction as mentioned above, many studies focus on related psychoacoustic effects. This includes the work by Alkmim et al., 10 who analyze the psychoacoustic metrics loudness, tonality, roughness, fluctuation strength, and sharpness from measurements on a quadrotor drone using a hemispherical microphone array. In their review on noise from unconventional aircraft, Lotinga et al. 11 give an overview on existing noise data for UAM, discuss psychoacoustic metrics, and state the importance of acoustic research on these types of emerging UAM, advanced air mobility, and unmanned aircraft system vehicles. König et al. 12 performed a digital user study, analyzing psychoacoustic metrics based on single propeller measurements as well as data from real flights with a drone. They found, among other things, that psychoacoustic metrics are well suited to describe drone noise annoyance and that the adaptation of technical and operational parameters can effectively reduce annoyance. In a recent work by Schade et al., 13 the psychoacoustic effects of a distributed propulsion system consisting of a UAM vehicle with 26 fans were analyzed based on measurements on three designs of a single fan. When compared with the noise from A320 turbofan engines at takeoff used in the comparison (IAE V2527-A5, Rolls Royce, Dahlewitz, Germany), significant reductions in tonality, roughness, and fluctuation strength were observed for two of the fan designs, while an increase in sharpness has been found for all designs.

As current studies imply that higher fan and motor speed may be required for electrified aircraft propulsion, <sup>14</sup> it is likely that high-frequency noise contributions from the electric motors will affect the noise from UAM vehicles, and especially psychoacoustic metrics such as sharpness. Several existing investigations already suggest that the electric machine contributes to the overall noise from the vehicle. <sup>15–17</sup>

The aim of the present paper is to assess the noise generated by the electric machine in a propulsion system of a conceptual UAM vehicle, driven by open propellers, using detailed numerical simulations as well as analytical models. In order to investigate the effect of rotational speed, torque, and size of the motor on the resulting noise radiation, a comparison is made for a direct drive version of the motor, which is directly coupled to the propeller, and a version that uses a gearbox to connect the motor with the propeller, reducing the high rotational speed of the motor shaft to that needed for the propeller. This assessment provides estimates of the equivalent radiated power (ERP) at distinct frequencies for the two different electric machines. The results can be useful for estimating the overall sound radiation of an electrified powertrain, particularly when combined with analytical models to predict propeller noise.<sup>18</sup>

The remainder of the paper is organized as follows: Important information on the design of the vehicle and its propulsion system are given in Sec. II. The following Sec. III then describes the calculation of the noise generated by electric motors, which refers to both numerical simulations (Sec. III A) as well as basic analytical models (Sec. III B). Results of these calculations are presented and compared in Sec. IV, and finally, a short summary and conclusion is given in Sec. V.

#### **II. PROPULSION SYSTEM DESIGN**

### A. Aircraft and propulsion system requirements

The conceptual UAM vehicle subject to the current study has a payload of 450 kg and is meant to carry a pilot and up to four passengers. The expected range is approximately 150 to 200 km, and the entry into service (EIS) is taken to be 2035. It was designed and sized using a methodology based on classical handbook techniques, which is derived from class II methods in conceptual aircraft and rotorcraft design. A more detailed description of this methodology can be found in the work of Shiva Prakasha et al. 19 The vehicle, a three-dimensional visualization of which is shown in Fig. 1, has eight electrically driven tiltable open rotors, two of which are mounted on the horizontal stabilizers. Table I shows the resulting top level aircraft requirements (TLAR).

The five-bladed propellers were designed using classical blade-element-momentum theory. 20,21 They have a diameter of 1.85 m and are designed to deliver the required thrust during hover and cruise flight, with tip Mach numbers



FIG. 1. Visualization of the electrically powered tilt-rotor vehicle.

TABLE I. Initial TLAR for the designed tilt-rotor vehicle.

Range	150–200 km (plus reserves)		
Flight speed	200–250 km/h		
MTOM	<3175 kg		
Payload	$450 \mathrm{kg} (1 \mathrm{pilot} + 4 \mathrm{passengers})$		
EIS	2030–2035		

of 0.521 and 0.300, respectively. Different topologies of the electric powertrain to drive the propellers have been designed.<sup>22</sup> They are all based on batteries and hydrogenpowered fuel cell systems but consider different hybridization factors. The result of this design step is the mass and the required power of the electric machines. This data forms the basis for the current analysis. Additional information on the conceptual design of the vehicle, the powertrain, and the propulsors can be found in the study by Schade et al.<sup>23</sup>

# B. Electric machine design

The electric machine is one of the key components in an electrified propulsion system. In order for electric motor designs to be applicable for aviation, a high power density (power per mass) as well as a high fault tolerance are necessary.<sup>24</sup> Currently, existing electrical machines for aircraft propulsion offer power densities in the range between 4 kW/ kg and 10 kW/kg. 14 Motor topologies of interest for aircraft propulsion include permanent magnet synchronous machines (PMSMs), superconducting machines, switched reluctance machines, and induction machines.<sup>25</sup> A further distinction can be made between inrunner and outrunner configurations. In an inrunner-type motor, the rotor, which houses the permanent magnets, is mounted on a shaft and rotates inside the stator. The shaft is then supported by bearings mounted to the casing that encloses the stator. In contrast, an outrunner configuration features stationary parts at the center of the machine, while the rotor rotates on the outside, often utilizing a bell structure or a rotating drum. This topology offers the advantage of allowing propeller blades to be mounted directly on the outside of the rotating drum, and air cooling of the permanent magnets is facilitated. Significant differences between these two topologies are anticipated in terms of structural vibrations.

Due to their high power density, high efficiency, and reliability,<sup>26</sup> radial flux PMSMs in inrunner configuration are selected in the current study. Thereby, two different options are considered: One is to design an electric machine that runs with the relatively low rotational speed required by the propeller, delivering the high torque directly. The second option is to design a faster running electric machine, which necessitates the use of an additional gearbox, but makes use of the fact that highly efficient electric machines are often designed to run very fast. For that reason, two distinct machines are designed and evaluated, one being a direct drive version (labeled "direct drive") and one a geared configuration (labeled "geared").

TABLE II. Speed and torque requirements for the two motor versions.

	Direct drive	Geared	
Rated speed (rpm) N <sub>r</sub>	1680	13 440	
Peak torque (Nm) T	852	106	
Peak power (kW) P	150	150	
Cooling	Air-cooled		

The machines are designed based on the necessary torque and rotational speed for both designs obtained from the propeller and powertrain requirements<sup>23</sup> using an open source tool.<sup>27</sup> They are given in Table II. As shown in Fig. 2, the output of this tool for a given set of operational input parameters like the required power, torque, and rotational speed are, among others, the dimensions of the rotor and the stator, the number of slots and poles, as well as the current.

For both the geared and the direct drive version of the motor, a variety of designs have been obtained using the open source tool based on variations of the direct current (DC) bus voltage, the current density, and the number of pole pairs. In a next step, the number of possible designs has been further refined by imposing additional constraints. For example, a rather small outer stator diameter of less than 300 mm is desired in order to enable the motor to be fitted into the rotor hub. In addition, it was decided to prefer motor designs with a maximum root mean square (rms) current density of  $10 \, \text{A/m}^2$ , as this will allow for the use of air cooling as opposed to an additional liquid cooling concept that may additionally increase the total mass and the complexity of the electric powertrain.

Finally, the two designs shown in Fig. 3 were selected. Table III gives an overview of some of the machine parameters. It becomes immediately visible that the direct drive version of the motor is much larger due to the greater

diameter and the longer lamination length, which are necessary to generate the high torque necessary to drive the large propeller. The geared version of the motor, on the other hand, is much smaller.

# III. NOISE CALCULATION

The noise from electric machines originates from a variety of different noise source mechanisms.<sup>28</sup> This includes noise generated by the magnetic field, leading to forces that excite the mechanical structure, as well as mechanically generated noise, aerodynamically generated noise (for example, due to additional cooling fans), as well as electronically generated noise due to switching harmonics from the inverter. In the current work, only the noise generated by the magnetic field between rotor and stator is analyzed, as it can be considered the dominant noise contribution. For each of the two motor designs, the magnetically induced noise, which is then radiated from the outer stator surface, is calculated using numerical simulations with a finite element analysis (FEA) solver. In addition, analytical models are used to obtain the radial flux density distribution in the air gap and to calculate eigenfrequencies.

It should be noted that analytical models for the calculation of electric motor noise are based on significant simplifications. For example, they typically neglect electric and magnetic saturation effects and effects of mechanical coupling between the rotor and stator. The insulation between the windings is commonly only considered as an additional mass, and instead of pulse-width modulation current signals, these models often assume pure sine signals. Another simplification is that in many models, only the normal component of the flux density is assumed to affect the noise generation, and hence, a potential effect of the tangential

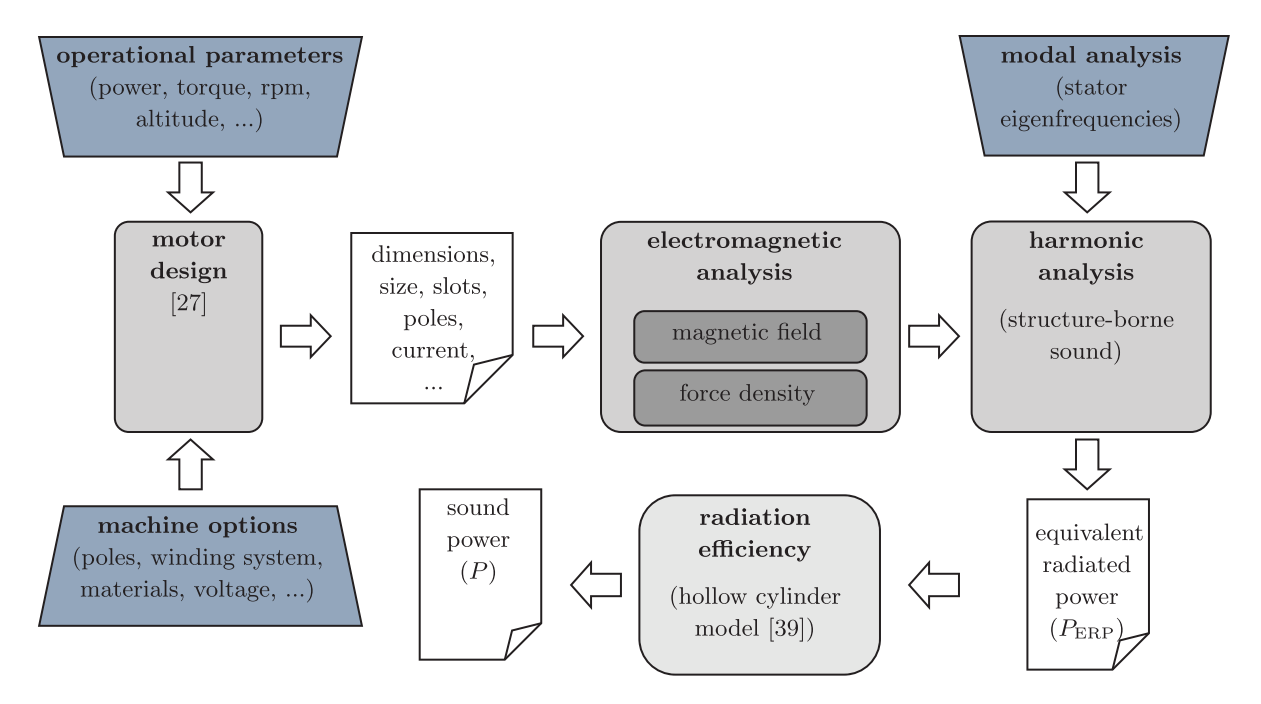


FIG. 2. Diagram of the workflow used to numerically determine the sound power.



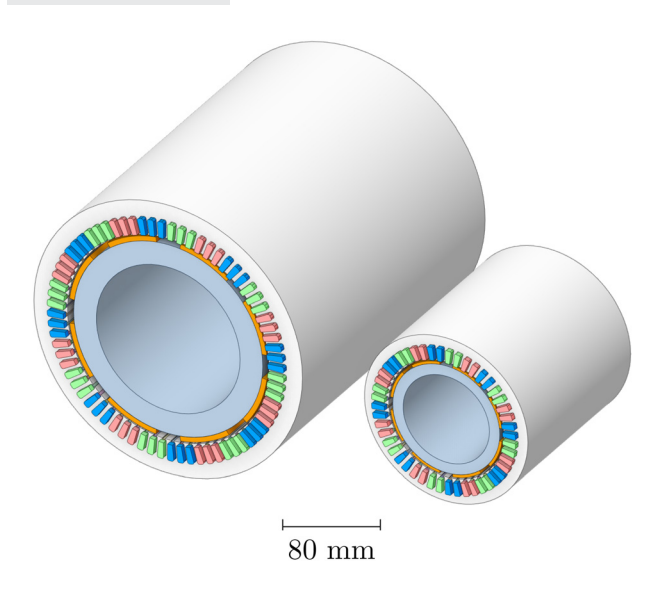


FIG. 3. Side-by-side comparison of the two electric machine designs (left: direct drive version; right: geared version).

component is completely neglected. Thus, in the current work, these models are only used for a first comparison of such estimations with the results from numerical simulations. A verification with experimental data is intended in a future phase of the study.

#### A. Numerical simulation

As shown in Fig. 2, in a first step, the resulting forces in the air gap must be determined. These are a function of the flux density in the radial and tangential direction  $B_{\rm rad}$  and  $B_{\rm tan}$ , respectively. The forces can then be prescribed to the teeth of the stator lamination in a second step in order to calculate the radiated power using a harmonic response analysis. This requires an additional modal analysis to be carried

TABLE III. Obtained machine parameters for both versions with a peak output power of  $150\,\mathrm{kW}$ .

	Direct drive	Geared
Number of slots N	72	48
Stator outer diameter (mm) $D_{1out}$	280	170
Stator bore diameter (mm) $D_{1in}$	210	120
Outer slot width (mm)	6.6	6.1
Inner slot width (mm)	5.1	4.2
Slot depth (mm) $h_{\rm sl}$	18.5	15.2
Slot opening (mm) $b_{14}$	2.8	2.1
Number of poles 2p	8	8
Magnet thickness (mm) $h_{\rm m}$	5	2.7
Magnet arc (EDeg)	123	126
Air gap height (mm) g	1.4	1.4
Rotor inner diameter (mm) $D_{2in}$	150	90
Lamination length (mm) l	330	185.6
Electric frequency (Hz) $f_e$	112	896
rms current density $(A/m^2) J$	10	10
Copper slot fill factor	0.53	0.57
Lamination stacking factor	0.95	0.95
DC bus voltage (V)	866	866

The radial vibration velocity on the surface of the stator caused by the excitation of the structure is then used to calculate the ERP. This is a simplified calculation of sound power based on plane wave propagation. The normal velocity at the stator surface  $v_n$  is used in place of the acoustic particle velocity, assuming the two are equal.

out beforehand in order to determine the eigenmodes and

In what follows, the steps of the simulation process will be explained in detail.

# 1. Electromagnetic calculation

The electromagnetic calculations have been performed based on the machine designs determined using the open source tool, with important parameters given in Table III. The pre-design tool outputs a number of geometrical and electrical parameters for each of the requested designs. By utilizing an application programming interface in Python, these parameters were used to build and simulate the machines using an FEA solver, Ansys Motor-CAD (ANSYS, Inc., Canonsburg, PA). This approach combines an analytically based pre-sizing method with numerical modeling of the machine.

Both machines have a single-layer, integral-slot winding system with three phases, which means that all conductors in a slot belong to a single phase. The number of slots per phase per pole q is given by

$$q = \frac{N}{2p \cdot m_{\rm ph}},\tag{1}$$

where N is the number of stator slots, p the number of pole pairs, and  $m_{\rm ph}$  the number of phases. In the direct drive version (Fig. 3, left), q=3 and 24 turns are wound per phase. In this case, 15 strands are used so that 30 conductors lie in one slot. Copper is used as the conductor material. Vacoflux 50 (VACUUMSCHMELZE GmbH & Co. KG, Hanau, Germany) is used for both the stator and rotor laminations, and Vacodym 238 TP (VACUUMSCHMELZE GmbH & Co. KG, Hanau, Germany) is used for the NdFeB permanent magnets with the magnetic flux density  $B_{\rm g}=1.248\,\rm T$ . For the geared version (Fig. 3, right) q=2 and 16 turns are wound per phase with 15 strands. For both designs, winding and magnet temperatures have been fixed to  $100\,^{\circ}$ C. At present, the models do not take into account the housing, cooling, shaft, or bearings.

Both machines are simulated for one electrical period, which is resolved with 48 points. Due to the given symmetry, it is sufficient to consider a pair of poles. This is resolved with a total of 5800 elements. The air gap is discretized with 288 elements in the circumferential direction and five layers in the radial direction, resulting in a good resolution for initial noise estimation.<sup>29</sup>

Figure 4 shows the torque as a function of rotational speed for the two machine designs investigated, while Fig. 5 shows the resulting magnetic field superimposed with lines of constant vector potential for the direct drive version.



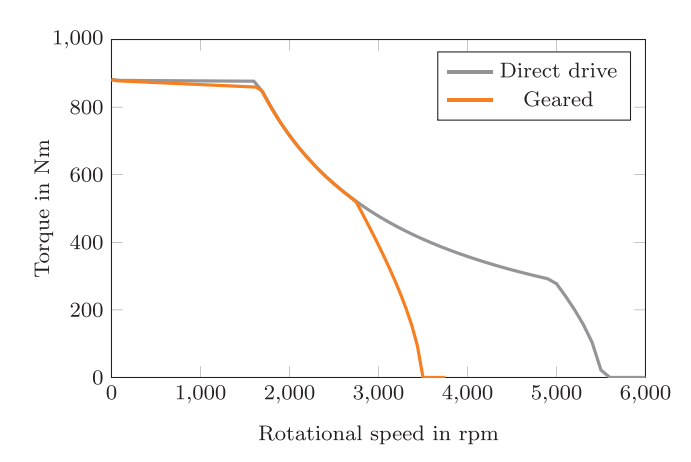


FIG. 4. Characteristic curves (torque as a function of rotational speed) of the two motor designs (note that for comparability, the values of the motor with gearbox have been applied to those acting on the propeller).

From the simulated magnetic fields for both motor designs, the magnetic flux densities in the air gap in radial and tangential direction,  $B_{\rm rad}$  and  $B_{\rm tan}$ , respectively, can be obtained. Subsequently, the radial and tangential components of the force density  $p_{\rm mag}(\alpha,t)$  as a function of time and electrical angle  $\alpha$  can be calculated as

$$p_{\rm rad}(\alpha, t) = \frac{1}{2\mu_0} \left[ B_{\rm rad}^2(\alpha, t) - B_{\rm tan}^2(\alpha, t) \right] \tag{2}$$

and

$$p_{\tan}(\alpha, t) = \frac{1}{\mu_0} \left[ B_{\text{rad}}^2(\alpha, t) B_{\tan}^2(\alpha, t) \right], \tag{3}$$

with  $\mu_0$  being the magnetic permeability. The force density can be understood as a magnetic pressure acting on a defined surface. In a next step, the forces F acting on the teeth can then be obtained using the acquired force densities,

$$F = p_{\text{mag}}(\alpha, t) l_{\text{arc}} l, \tag{4}$$

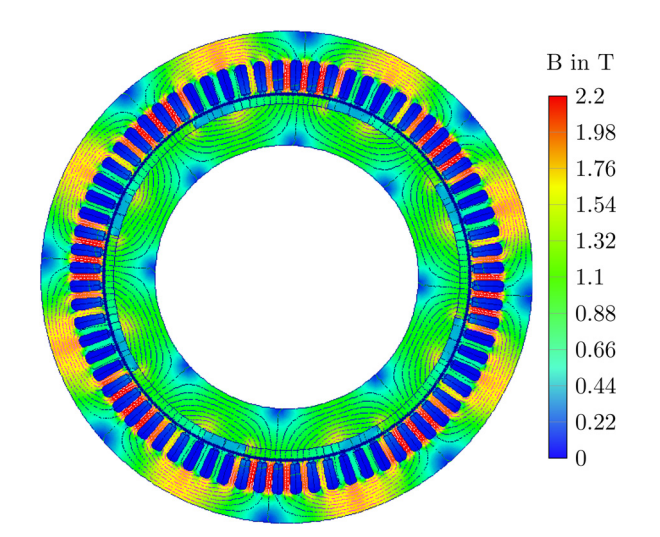


FIG. 5. Flux density with equipotential lines for the direct drive version (result for a single pole pair has been duplicated to form whole machine).

where l is the lamination length, and  $l_{\rm arc}$  is the length of the arc the force is acting on. Assuming the tangential contributions to the force density are small compared to the radial contributions,  $p_{\rm mag}(\alpha,t)$  approximately corresponds to  $p_{\rm rad}(\alpha,t)$ .

# 2. Modal analysis

If the frequencies of the electromagnetic forces, described in Sec. III A 1, are close to the natural frequencies of the stator, significant vibrations are induced and, consequently, considerable noise is radiated.<sup>30</sup> Thus, it is imperative to assess the eigenfrequencies of the stator.

For the numerical modal analysis, a total of 134000 mesh elements were used for the direct drive version and 163000 mesh elements for the geared version. The stator lamination material has a Young's modulus  $E=215\,\mathrm{GPa}$ , a density  $\rho_\mathrm{m}=8120\,\mathrm{kg/m^3}$  and a Poisson's ratio  $\nu=0.3$ . No boundary conditions were specified that would fix the stator.

#### 3. Harmonic response

The forces from the electromagnetic analysis at rated speed  $N_{\rm r}$  are used as input excitation for the harmonic response calculation. At these frequencies, the resulting surface normal steady-state velocity  $v_{\rm n}$  is integrated over the stator outer surface A to obtain the ERP

$$P_{\rm ERP} = \frac{\rho_0 c_0}{2} \int_A \hat{v}_{\rm n}^2 dA.$$
 (5)

In Eq. (5),  $\rho_0$  is the density of the surrounding fluid,  $c_0$  is the speed of sound, and  $\hat{v}_n$  is the amplitude of the normal vibration velocity on the structure.

As mentioned previously, this is a simplified estimation of the radiated sound power. The ERP typically overestimates the radiated sound at lower frequencies yet provides a qualitatively accurate approximation for structure-induced acoustic fields.<sup>31</sup> High ERP levels give a first indication of potentially critical acoustic frequency ranges because they occur when frequencies belonging to maxima of the magnetic force are close to an eigenfrequency of the stator structure.

For improved accuracy, the frequency-dependent radiation efficiency factor  $\sigma$  can be introduced, and the sound power can subsequently be calculated as

$$P = \sigma(f) P_{\text{ERP}}. \tag{6}$$

The radiation efficiency is defined as the real part of the so-called radiation impedance and describes the correlation between the vibrations of the cylindrical shell and the factually radiated sound power.<sup>32,33</sup> It typically ranges between 0 and 1, although values greater than 1 are also possible. A low valued radiation efficiency means that only a small portion of the vibrational energy will be radiated into the surrounding medium in the form of sound waves, while a high value means a high degree of sound radiation. Local

acoustic effects are thereby taken into account. Section III B on the analytical calculation of noise from electric machines provides additional information on the calculation of the radiation efficiency of hollow cylinders as a simplified model for a stator of an inrunner PMSM.

### B. Analytical calculation

In addition to the numerical method presented in Sec. III A, this section outlines an analytical approach for the estimation of the noise radiated by a PMSM. Thereby, the approach is basically similar to that used for the numerical simulation: In a first step, the forces caused by the magnetic flux density in the air gap are calculated. In a second step, a structural-mechanical analysis is performed in order to obtain the eigenfrequencies of the stator. Finally, the radiated noise from the stator of the electric motor is calculated.

# 1. Forces in the air gap

For the analytical approximation of the sound radiated by the electric motor, the force amplitude of the circumferential mode m can be approximated as

$$F_{\rm m} = \pi D_{\rm lin} l \hat{p}_{\rm r},\tag{7}$$

with  $D_{1\rm in}$  the inner (or bore) diameter of the stator and  $\hat{p}_r$  the amplitude of the magnetic force per unit area with the space order r. When only circumferential modes m are considered, the force component of order r exclusively excites the mode of the same order, where r=m.<sup>30</sup>

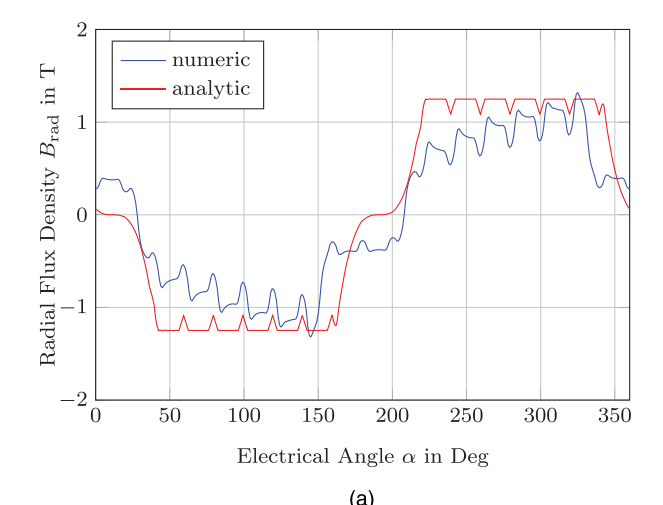
Similar to the numerical simulation and under the assumption that  $B_{\rm tan} \ll B_{\rm rad}$ , the spatial distribution of the magnetically induced pressure in the air gap can be estimated as

$$p_{\rm r}(\alpha, t) \approx p_{\rm rad}(\alpha, t) \approx \frac{1}{2\mu_0} B_{\rm rad}^2(\alpha, t).$$
 (8)

The magnetic flux density in the air gap for PMSM can be approximated as the sum of the magnetic field produced by the magnets on the rotor and that produced by the coils at the stator. Due to the complex solution of the Maxwell stress tensor for magnetic fields, an analytic approach using a Fourier series constitutes a fast method to calculate the magnetic flux density as

$$B_{\rm rad}(\alpha) = \underbrace{\frac{1}{k_{\rm c}} \sum_{\phi} B_{\rm g} b_{\phi} k_{{\rm s}\phi} \cos(\phi \alpha)}_{\text{flux of the permanent magnets}} \\ - \underbrace{\frac{2\gamma g}{t_1} \sum_{\rm k=1}^{\infty} k_{0{\rm k}}^2 k_{\rm sk}^2 \cos\left(\frac{k2\alpha\tau}{t_1}\right) \sum_{\phi} B_{\rm g} b_{\phi} k_{{\rm s}\phi} \cos(\phi \alpha)}_{\text{flux of the coils}}, \tag{9}$$

with  $k_c$  being the carter coefficient,  $B_g$  the magnetic flux density of the permanent magnets,  $b_{\phi}$  the coefficient of the



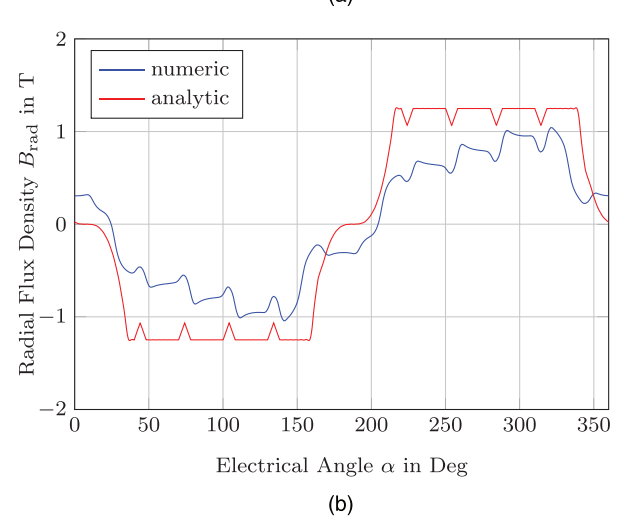


FIG. 6. Radial flux density in the center of the air gap for the two configurations at a fixed time *t*, obtained using analytical and numerical methods. (a) Direct drive, (b) geared version.

Fourier series higher space harmonics,  $k_{s\phi}$  the rotor permanent magnet skew factor,  $\phi$  the higher space harmonics,  $\tau$  the pole pitch,  $\gamma$  a constant depending on slot opening and air gap,<sup>34</sup>  $t_1$  the stator slot pitch, g the air gap height, and  $k=1, 2, 3, \ldots$  The variable  $k_{0k}$  represents the stator slot opening coefficient, and  $k_{sk}$  defines the stator slot skew factor.

Figure 6 shows a comparison of the radial flux density in the air gap obtained using the numerical and the analytical approach for both machine designs. It can be observed that the overall shape is in good agreement, but the analytical results appear to omit some features. The results obtained through numerical simulation show an increase in amplitude of the magnetic flux density at each pole as the electrical angle increases, for example, from 200 to 320 electrical degrees. Conversely, the flux density for the analytical approach is capped at a maximum value. Still, the north and south pole of the pole pair are clearly visible in the numerically obtained data and that from the analytical calculation, and both approaches are able to account for the number of stator slots (18 over the course of 360 electrical

degrees for the case with the direct drive, 12 for the geared version), although the effect of the slots is more pronounced in the data obtained via simulation.

Substituting Eq. (9) into Eq. (8) yields the magnetic force per unit area, which is needed to calculate the vibration velocity  $v_{\rm m}$  of the mode m for the stator outer surface. The vibration velocity can then be calculated as

$$v_{\rm m} = \omega_{\rm r} d_{\rm m} = 2\pi f_{\rm r} \frac{\pi D_{\rm 1in} l}{M_{\rm s} \omega_{\rm m}^2} P_{\rm mr} h_{\rm m},$$
 (10)

where  $f_{\rm r}$  and  $\omega_{\rm r}$  are the frequency and the circular frequency of the force component with the order r. The variable  $M_{\rm s}$  is the mass of the stator,  $\omega_{\rm m}=2\pi f_{\rm m}$  is the eigenfrequency of the mode m,  $d_{\rm m}$  is the radial vibration displacement, and  $h_{\rm m}$  is a magnification factor. This magnification factor depends on the modal damping factor, which is frequency-dependent and can be determined via modal analysis or estimated using, for example, empirical relations. <sup>30</sup>

# 2. Stator eigenfrequencies

This section describes an analytical approach to estimate the eigenfrequencies of the stator for the case that both ends of the shell are free. The geometry of such a stator of a radial flux PMSM can be considered as a cylindrical shell with the (lamination) length l, an outer radius  $r_{\rm o}$  ( $r_{\rm o}=0.5\cdot D_{\rm lout}$ ) and a wall thickness h, which is calculated based on the difference between outer diameter  $D_{\rm lout}$  and inner diameter  $D_{\rm lin}$  of the stator. In a first step, the eigenfrequencies of such a simple cylindrical shell are calculated. In a second step, the effect of the stator teeth on the vibrational response of the stator is considered by the introduction of a factor accounting for the relative increase in mass due to the stator teeth.

The calculation used in the present paper is based on simple approximations for a so-called thick-walled cylindrical shell,  $^{35}$  meaning that the ratio of its wall thickness to its inner diameter  $h/r_{\rm i} > 1/20$ . The estimation of the eigenfrequencies of such a cylinder is based on a corresponding calculation of the eigenfrequencies for thinwalled cylindrical shells and so-called "equivalent plates," where the shell is cut along its length and unfurled. This leads to

$$f_{\rm nm} = f_{\rm ring} \frac{\Omega_{\rm nm,t} \Omega_{\rm nm,p}}{\eta^2 \sqrt{\delta}},\tag{11}$$

where  $\Omega_{\text{nm,t}}$  represents eigenfrequencies of a thin-walled cylinder of axial mode n and circumferential mode m,

$$f_{\rm nm} = f_{\rm ring} \sqrt{\frac{(1-\nu^2)x^4 + \delta A'}{(x^2+m^2)^2 + m^2}},$$
 (12)

divided by the ring frequency

$$f_{\rm ring} = \frac{c_{\rm L}}{2\pi r_{\rm c}} = \frac{1}{2\pi r_{\rm c}} \sqrt{\frac{E}{\rho_{\rm m}(1-\nu^2)}}.$$
 (13)

In Eq. (11),  $\Omega_{nm,p}$  represents the normalized eigenfrequencies of the equivalent plate, which can be approximated by the lower of the two real valued solutions of

$$\Omega_{\rm nm}^4 - \Omega_{\rm nm}^2 \left(\frac{\zeta}{\delta} + (1+\zeta)\eta^2\right) + \zeta\eta^4 = 0. \tag{14}$$

In these equations,  $c_{\rm L}=\sqrt{E/[\rho_{\rm m}(1-\nu^2)]}$  is the longitudinal wave velocity,  $\rho_{\rm m}$  the density of the material, and  $r_{\rm c}=r_{\rm o}-0.5h$  the medial radius of the cylinder. Furthermore,  $r_{\rm o}$  constitutes the outer radius and the variable

$$x = k_{\rm a} r_{\rm o} = \left(n - \frac{1}{2}\right) \frac{\pi r_{\rm o}}{l} \tag{15}$$

constitutes a dimensionless axial wave number. Note, that simply supported or clamped mounting conditions can be incorporated by using the respective axial wave numbers  $k_a$ ; see, for example, the study by Wang and Lai. The variable  $\delta$  is defined as

$$\delta = \frac{h^2}{12r_o^2},\tag{16}$$

and the variable A' as

$$A' = (x^2 + m^2)^4 - 2[\nu x^6 + 3x^4 m^2 + (4 - \nu)x^2 m^4 - (2 - \nu)x^2 m^2 + m^6] + m^4.$$
 (17)

The dimensionless quantity  $\zeta$  is defined as

$$\zeta = \frac{1 - \nu}{2\kappa}, \quad \text{with } \kappa \approx 1.2,$$
 (18)

and  $\eta = k_{\rm ep} r_{\rm c}$  is the dimensionless wave number of the equivalent plate with

$$k_{\rm ep} = \sqrt{k_{\rm x}^2 + k_{\rm y}^2},$$
 (19)

where  $k_x = m/r_c$  and  $k_y = k_a = (n - 1/2)(\pi/l)$  represent the wave numbers in the x and y direction, respectively.

Still, applying Eq. (11) to calculate the eigenfrequencies of the stator of a PMSM will introduce errors. The teeth and windings of the stator constitute a deviation from the cylindrical shell geometry as well as an increase in mass and stiffness. Neglecting the change of stiffness as well as the mass of the windings under the assumptions that the change of stiffness is small compared to the change of mass, and that the mass of the windings is small compared to the mass of the stator teeth, a correction factor  $\kappa_{\rm m}$  is introduced in the current study to compensate for the added mass of the teeth. This results in a decrease in the natural frequencies according to

$$\kappa_{\rm m} = \frac{M_{\rm s}}{M_{\rm c}},\tag{20}$$

where  $M_s$  represents the mass of the stator, i.e., the sum of the mass of the hollow cylinder and the added mass of the teeth and  $M_c$  the sole mass of the hollow cylinder. A similar approach is often used in the vibrational analysis of stator systems. The factor is incorporated into a corrected ring frequency according to

$$f_{\rm ring} = \frac{c_{\rm L}}{2\pi r_{\rm c}\sqrt{\kappa_{\rm m}}} = \frac{1}{2\pi r_{\rm c}}\sqrt{\frac{E}{\rho_{\rm m}\kappa_{\rm m}(1-\nu^2)}}.$$
 (21)

The assumption made implies that change of the inertial properties, i.e., the change of mass, of the cylindrical shell has to considerably outweigh its change of the stiffness. In reality, however, the stiffness of the geometry is also impacted by the stator teeth. An increased stiffness would result in a shift of the eigenfrequencies to higher frequencies. Yet, the effect on the stiffness is expected to be small compared to the effect on the mass for most stator configurations. Thus, in the present work, the eigenfrequencies of the stator of both motor versions are calculated analytically using Eq. (11) together with Eq. (21).

# 3. Radiation efficiency

As mentioned before, the sound radiation of solid structures is characterized by the modal radiation efficiency  $\sigma_{nm}.$  Assuming a point-like excitation, the radiation efficiency of hollow thick-walled cylinders can be calculated by considering the circumferential modes only. Hence,  $\sigma_{nm} \approx \sigma_m$  with

$$\sigma_{\rm m} = \begin{cases} 0 & \text{if } \frac{2\pi}{\lambda_{\rm z}} > k_0, \\ \frac{2k_0}{\pi k_{\rm r}^2 r_0 |H_{\rm m}^{(2)'}(k_{\rm r}r_0)|^2} & \text{if } \frac{2\pi}{\lambda_{\rm z}} < k_0, \end{cases}$$
(22)

where  $|H_{\rm m}^{(2)}{}'(k_{\rm r}r_{\rm o})|$  represents the first derivative of the Hankel function of the second kind and order m. The variable  $\lambda_{\rm z}$  defines the longitudinal wavelength,  $k_0=\omega/c_0$  the acoustic wave number in the medium surrounding the shell, and  $k_{\rm r}$  the wave number in radial direction, defined as

$$k_{\rm r} = \sqrt{k_0^2 - \left(\frac{n\pi}{l}\right)^2}.\tag{23}$$

From Eq. (22), it is seen that the vibrations are only translated into radiating sound waves if the longitudinal wave numbers of the vibrations are smaller than the wave number of the surrounding medium. The radiation efficiency can be applied to Eq. (5) to obtain the sound power from the ERP.

Using the hollow cylinder model, actual values of radiation efficiency can be calculated as a function of frequency and mode shape. Applying these to the ERP values obtained in the previous step can give more precise results for the radiated sound power, especially at lower frequencies.

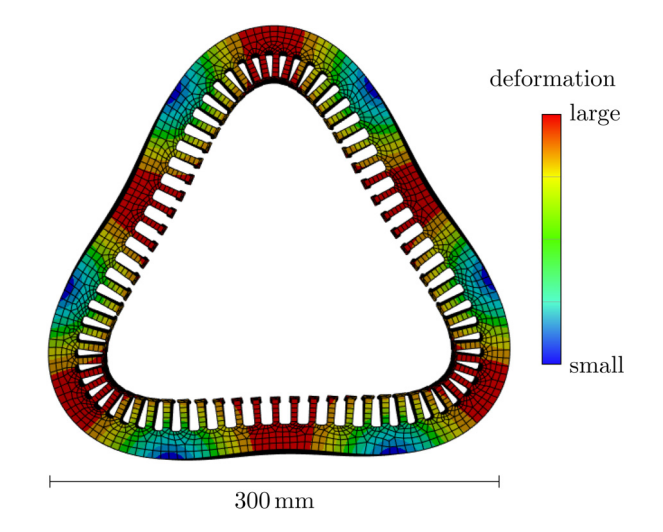


FIG. 7. Exemplary visualization of the deformation at a selected eigenmode  $(m=3, n=0, f=1438 \, \text{Hz})$  of the stator of the direct drive version.

#### IV. RESULTS AND DISCUSSION

In the current section, results from both the numerical simulations and the analytical models are presented, starting with the eigenfrequencies of the stator. As both stator configurations can be classified as thick-walled cylindrical shells, their eigenfrequencies are calculated by Eq. (11).

As a first qualitative example, Fig. 7 shows the deformation of one of the numerically obtained eigenmodes  $(f = 1438 \,\mathrm{Hz})$  for the stator of the direct drive variant. It is the circumferential mode with m=3 and n=0. In Table IV, the numerically calculated eigenfrequencies and the ones estimated analytically using Eq. (11) and Eq. (20) are compared. The results show a good agreement, considering the simplifications and assumptions used in the analytical calculation. For the plain circumferential modes where n = 0, differences are below 6%. With the exception of mode m=4 in the geared version, the analytical model underpredicts the eigenfrequencies by a small margin. However, for the longitudinal modes with n = 1, a larger deviation between numerical calculation and approximation is visible for both configurations. A possible explanation might be that the sole consideration of the mass of the stator teeth is not sufficient to capture all the details and that the absence of the stator teeth in the analytical model leads to the aforementioned differences.

TABLE IV. Comparison of eigenfrequencies obtained from modal analysis (Sec. III A 2) and analytical method (Sec. III B 2), based on data from Table III.

Mode indices		Direct drive		Geared	
m	n	Numerical	Analytical	Numerical	Analytical
2	0	525 Hz	499 Hz	807 Hz	775 Hz
2	1	657 Hz	692 Hz	1056 Hz	1150 Hz
3	0	1438 Hz	1391 Hz	2183 Hz	2162 Hz
3	1	1625 Hz	1473 Hz	2553 Hz	2322 Hz
4	0	2652 Hz	2620 Hz	3962 Hz	4071 Hz



As the noise radiated by the stator into the far field is affected not only by the ERP but also by the radiation efficiency of the stator, Fig. 8 shows the radiation efficiency calculated according to Eq. (22). The radiation efficiency is generally low, if the wavelength of the radial vibration is large compared to the outer radius of the cylindrical shell. The ratio of outer radius and wavelength, where the radiation efficiency becomes significant, increases with increasing circumferential mode number m.

Finally, as a measure for the noise generated due to magnetically induced forces in the air gap, Fig. 9(a) shows the numerically calculated ERP-level for the first 22 multiples of the electric frequency  $f_{\rm e}$  for both configurations. The comparison is made for all orders of  $f_e$  for the geared motor where the frequency is below 20 kHz. For both motor versions, only the harmonics of the second order contribute significantly to surface vibrations of the cylinder shell and, therefore, to the ERP. It is immediately visible that the levels are considerably higher for the geared motor for the first 14 motor orders. The highest level of 73.6 dB occurs at motor order 10, with a notable level difference to the direct drive version of around 40 dB. For higher motor orders, the ERP of the geared motor is below that of the direct drive. In total, the overall ERP level for the first 22 orders is 64.0 dB for the direct drive and 74.8 dB for the geared motor.

Figure 9(b) shows the same ERP level, but as a function of frequency. Now, as the rated speed is eight times higher for the geared motor, the electromagnetic forces are shifted towards higher frequencies and, consequently, the multiples of the electric frequencies also increase by the same factor. The largest ERP levels occur for the geared motor at 2 kHz and 9 kHz. These frequencies are located well above the blade passing frequency of the rotor and are, therefore, most likely not masked and well distinguishable from the rotor noise. Moreover, as shown in Fig. 8, the diameter of the stator as well as the frequency strongly affect the radiation efficiency. Towards large  $k_r r_0$ , the radiation factor  $\sigma_{\rm m}$  becomes one, meaning that larger structures can radiate sound more effectively at lower frequencies, but also that higher frequencies are generally radiated very effectively. In this case,

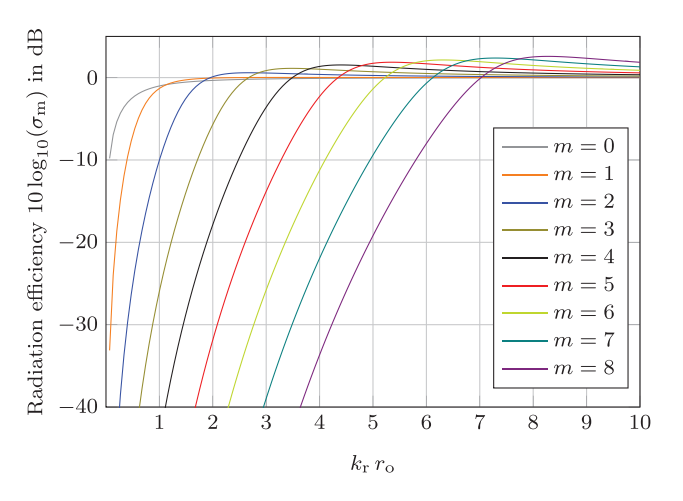
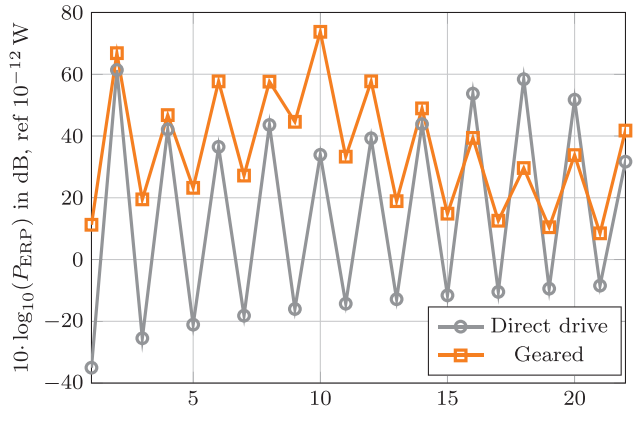


FIG. 8. Radiation efficiency according to Eq. (22).



Order of electrical frequency  $f_{\rm e}$ 

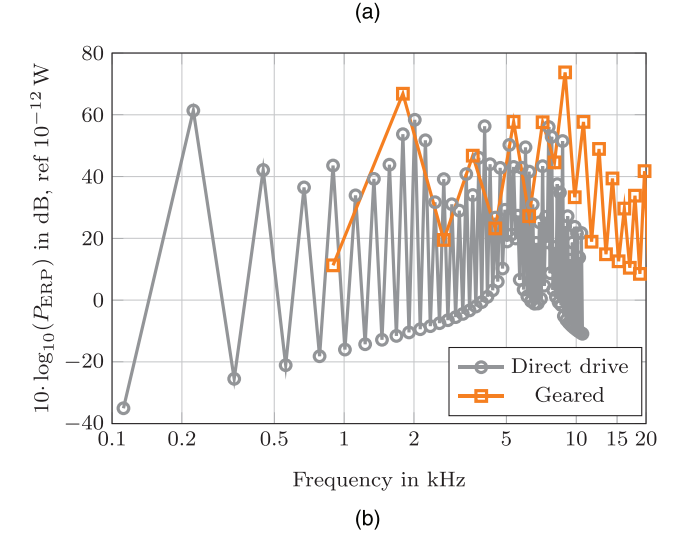


FIG. 9. Equivalent radiated power of the stator cylinder outer surface as a function of order of electric frequency and frequency for both configurations at rated speeds.

the ratio of the rated speeds is much higher than the ratio of the motor diameters so that the high ERP levels at high frequencies will become even more relevant because the radiation factor is close to one.

These findings indicate that, for the present use case, the direct drive motor seems acoustically more favorable, although components such as casings, windings, bearings, shafts, as well as the general integration of the electric machine into a propulsion unit and, subsequently, into an aircraft, have been omitted from the analysis. This omission may also affect the radiation efficiency, and hence, the current study focuses on the effective perceived power levels instead of noise radiated into the acoustic far field. In addition, other important properties of the two electric motors were not considered as well. This includes, for example, the total mass, which of course plays a significant role when designing propulsion systems for novel UAM vehicles.

In general, high output powers, which are required for efficient electric machines in aviation, can be achieved by high torque or a high rotational speed. Increasing the torque requires increasing the machine diameter or the lamination length, which could lead to mechanical issues and, more important, is in conflict with the request for lightweight design and a high power-to-weight ratio. Thus, increasing the rotational speed is a promising option to meet the required power specifications, enabling the use of smaller-sized electric machines with high rotational speeds. However, such designs will lead to the generation of high-frequency noise, which in turn is likely to contribute to the total noise of UAM vehicles, especially when the noise from the propulsors is in a different range of frequencies. <sup>18</sup>

#### V. CONCLUSION

The current paper describes the assessment of the noise, i.e., the ERP at distinct frequencies, for two different electric machines for an electrically powered UAM vehicle. It focuses on the noise that is generated due to forces acting on the structure caused by the magnetic field inside the air gap between rotor and stator.

The chosen concept vehicle, which is intended to carry five persons over a range of up to 200 km, is powered by eight tiltable open rotors, each driven by a PMSM. In order to analyze the effects of certain motor design parameters, two different electric machine versions were designed, one as a direct drive and one that requires an additional gear box. This leads to notable differences in the motor dimensions, but also—due to the fact that the latter rotates much faster—to difference in the spectral shape of the resulting magnetic forces and, subsequently, the radiated noise.

This is confirmed by the results from the numerical simulations. They show that, in general, both electric machines lead to levels of the ERP with maximum values on the order of 60 dB and above, with the geared version reaching peak values of more than 70 dB at high frequencies above 8 kHz. Considering that noise is radiated more efficiently at high frequencies, as illustrated by a radiation efficiency of one at high frequencies, and assuming that the aerodynamic noise from the open rotors occurs mainly at low and medium frequencies, an increase in the total noise is likely for electric machines with high rotational speeds. In addition, such high-frequency contributions will also affect psychoacoustic metrics such as sharpness. This will lead to the fact that noise from UAM vehicles will be perceived as more annoying due to the contribution of the electric motor.

It should be noted, however, that the current study does not take into account the mounting of the electric machine, meaning that no structural components at either end of the stator or the rotor shaft have been included. It is known that such elements can potentially have a strong impact on the eigenmodes and eigenfrequencies. <sup>40</sup> These effects are also not captured by the analytical equations presented in the current paper. In addition, a possible shielding effect of the nacelle as well as a sound transmission loss due to the enclosure have been neglected for simplicity.

#### **ACKNOWLEDGMENTS**

The authors thank Patrick Ratei (German Aerospace Center, Institute of System Architectures in Aeronautics), Jonas Ludowicy, Vivek Gupta, and Julia Genßler (German Aerospace Center, Institute of Electrified Aero Engines) for their valuable input. This publication is part of the project VIRLWINT (Virtual acoustic twin of distributed propulsion systems) funded by the German Aerospace Center.

# AUTHOR DECLARATIONS Conflict of Interest

The authors state that they have no conflicts to disclose.

### **DATA AVAILABILITY**

The data that support the findings of this study are available from the corresponding author upon reasonable request

- <sup>1</sup>A. Straubinger, R. Rothfeld, M. Shamiyeh, K.-D. Büchter, J. Kaiser, and K. O. Plötner, "An overview of current research and developments in urban air mobility–setting the scene for UAM introduction," J. Air Transp. Manage. 87, 101852 (2020).
- <sup>2</sup>A. Brown and W. L. Harris, "Vehicle design and optimization model for urban air mobility," J. Aircraft **57**(6), 1003–1013 (2020).
- <sup>3</sup>W. Johnson and C. Silva, "NASA concept vehicles and the engineering of advanced air mobility aircraft," Aeronaut. J. **126**(1295), 59–91 (2022).
- <sup>4</sup>S. K. S. Whiteside, B. P. Pollard, K. R. Antcliff, N. S. Zawodny, X. Fei, C. Silva, and G. L. Medina, "Design of a tiltwing concept vehicle for urban air mobility," Report No. NASA/TM–20210017971, NASA, Washington, DC (2021).
- <sup>5</sup>S. K. S. Whiteside and B. P. Pollard, "Conceptual design of a tiltduct reference vehicle for urban air mobility," in *Proceedings of the Aeromechanics for Advanced Vertical Flight Technical Meeting, Transformative Vertical Flight 2022*, San Jose, CA (January 25–27, 2022).
- <sup>6</sup>S. A. Rizzi, D. L. Huff, D. D. Boyd, P. Bent, B. S. Henderson, K. A. Pascioni, D. C. Sargent, D. L. Josephson, M. Marsan, H. B. He, and R. Snider, "Urban air mobility noise: Current practice, gaps, and recommendations," Report No. NASA/TP–2020-5007433, NASA, Washington, DC (2020).
- <sup>7</sup>D. S. Little, J. Majdalani, R. J. Hartfield, and V. Ahuja, "On the prediction of noise generated by urban air mobility (UAM) vehicles. I. Integration of fundamental acoustic metrics," Phys. Fluids **34**(11), 116117 (2022).
- <sup>8</sup>V. Ahuja, D. S. Little, J. Majdalani, and R. J. Hartfield, "On the prediction of noise generated by urban air mobility (UAM) vehicles. II. Implementation of the Farassat F1A formulation into a modern surface-vorticity panel solver," Phys. Fluids **34**(11), 116118 (2022).
- <sup>9</sup>J. Ko, B. J. German, and J. Rauleder, "Noise assessment of multirotor configurations during landing procedures," J. Acoust. Soc. Am. **156**(6), 3741–3756 (2024).
- <sup>10</sup>M. Alkmim, J. Cardenuto, E. Tengan, T. Dietzen, T. Van Waterschoot, J. Cuenca, L. De Ryck, and W. Desmet, "Drone noise directivity and psychoacoustic evaluation using a hemispherical microphone array," J. Acoust. Soc. Am. 152(5), 2735–2745 (2022).
- <sup>11</sup>M. J. Lotinga, C. Ramos-Romero, N. Green, and A. J. Torija, "Noise from unconventional aircraft: A review of current measurement techniques, psychoacoustics, metrics and regulation," Curr. Pollut. Rep. 9(4), 724–745 (2023).
- <sup>12</sup>R. König, L. Babetto, A. Gerlach, J. Fels, and E. Stumpf, "Prediction of perceived annoyance caused by an electric drone noise through its technical, operational, and psychoacoustic parameters," J. Acoust. Soc. Am. 156(3), 1929–1941 (2024).
- <sup>13</sup>S. Schade, R. Merino-Martinez, A. Moreau, S. Bartels, and R. Jaron, "Psychoacoustic evaluation of different fan designs for an urban air mobility vehicle with distributed propulsion system," J. Acoust. Soc. Am. 157(3), 2150–2167 (2025).
- <sup>14</sup>R. C. Bolam, Y. Vagapov, and A. Anuchin, "A review of electrical motor topologies for aircraft propulsion," in *Proceedings of the 55th International Universities Power Engineering Conference (UPEC)*, Turin, Italy (September 1–4, 2020).



- <sup>15</sup>D. L. Huff, B. S. Henderson, and E. Envia, "Motor noise for electric powered aircraft," in Proceedings of the 22nd AIAA/CEAS Aeroacoustics Conference, Lyon, France (May 30-June 1, 2016).
- <sup>16</sup>D. L. Huff and B. S. Henderson, "Electric motor noise for small quadcopters: Part 1-Acoustic measurements," in Proceedings of the 2018 AIAA/ CEAS Aeroacoustics Conference, Atlanta, GA (June 25–29, 2018).
- <sup>17</sup>B. S. Henderson, J. Cluts, A. A. Svetgoff, J. Jantzen, and J. Bennett, "Acoustic measurements for the Moog S-250 vehicle in hover," in Proceedings of the 30th AIAA/CEAS Aeroacoustics Conference, Rome, Italy (June 4-7, 2024).
- <sup>18</sup>E. W. Schneehagen, S. Hakansson, V. Gupta, A. Lopez Pulzovan, and T. F. Geyer, "Initial comparison of noise emissions of distributed electric propulsion systems for a regional aircraft," in Proceedings of the AIAA Aviation Forum and ASCEND 2025, Las Vegas, NV (July 21-25, 2025).
- <sup>19</sup>P. Shiva Prakasha, N. Naeem, P. Ratei, and B. Nagel, "Aircraft architecture and fleet assessment framework for urban air mobility using a system of systems approach," Aerosp. Sci. Technol. 125, 107072 (2022).
- <sup>20</sup>R. Eppler and M. Hepperle, "A procedure for propeller design by inverse methods," in Proceedings of the International Conference on Inverse Design Concepts in Engineering Sciences (ICIDES), Austin, TX (October 17-18, 1984), edited by G. S. Dulikravich, pp. 445-460.
- <sup>21</sup>M. Hepperle, "Inverse aerodynamic design procedure for propellers having a prescribed chord-length distribution," J. Aircraft 47(6), 1867–1871 (2010).
- <sup>22</sup>J. Ludowicy, P. Ratei, and S. de Graaf, "Comparison of energy sources for an electric powertrain in a tilt-rotor urban air mobility vehicle," Eng. Proc. 90(1), 69 (2025).
- <sup>23</sup>S. Schade, J. Ludowicy, P. Ratei, M. Hepperle, A. Stürmer, K.-S. Rossignol, S. de Graaf, and T. F. Geyer, "Conceptual design of electrically-powered urban air mobility vehicles for aeroacoustic studies," in Proceedings of the Deutscher Luft- und Raumfahrtkongress (DLRK), Hamburg, Germany (September 30-October 2, 2024).
- <sup>24</sup>Y. Wang, C. Zhang, C. Zhang, and L. Li, "Review of high-power-density and fault-tolerant design of propulsion motors for electric aircraft," Energies 16(19), 7015 (2023).
- <sup>25</sup>Y. Wang, "Full electric aircraft and the electrical motors of the propulsion systems," Highlights Sci. Eng. Technol. 103, 340-347 (2024).
- <sup>26</sup>E. Teichert and S. Kazula, "Overview and evaluation of electric machines for electric regional aircraft propulsion systems," in Proceedings of the

- Deutscher Luft- und Raumfahrtkongress (DLRK), Hamburg, Germany (September 30-October 2, 2024).
- <sup>27</sup>S. Kalt, J. Erhard, and M. Lienkamp, "Electric machine design tool for permanent magnet synchronous machines and induction machines," Machines 8(1), 15 (2020).
- <sup>28</sup>P. Vijayraghavan and R. Krishnan, "Noise in electric machines: A review," IEEE Trans. Ind. Appl. 35(5), 1007-1013 (1999).
- <sup>29</sup>S. Hakansson and T. F. Geyer, "Studying the influence of parameters in a lumped tooth force based noise assessment of a permanent magnet synchronous machine," in Proceedings of DAS|DAGA 2025, Copenhagen, Denmark (March 17-20, 2025), pp. 1446-1449.
- <sup>30</sup>J. Gieras, C. Wang, and J. Lai, Noise of Polyphase Electric Motors (Taylor & Francis Group, London, UK, 2005).
- <sup>31</sup>D. Fritze, S. Marburg, and H.-J. Hardtke, "Estimation of radiated sound power: A case study on common approximation methods," Acta Acust. united Ac. 95(5), 833-842 (2009).
- <sup>32</sup>M. C. Junger, "Radiation loading of cylindrical and spherical surfaces," J. Acoust. Soc. Am. 24(3), 288-289 (1952).
- <sup>33</sup>M. C. Junger, "The physical interpretation of the expression for an outgoing wave in cylindrical coordinates," J. Acoust. Soc. Am. 25(1), 40-47 (1953).
- <sup>34</sup>J. F. Gieras, "Analytical approach to cogging torque calculation of PM brushless motors," IEEE Trans. Ind. Appl. 40(5), 1310–1316 (2004).
- <sup>35</sup>D. Guicking and R. Boisch, "Vereinfachte Berechnung der Eigenfrequenzen dickwandiger Zylinder in Luft und Wasser" ("Simplified calculation of natural frequencies of thick-walled cylinders in air and water"), Acustica 42(21), 89-97 (1979).
- <sup>36</sup>C. Wang and J. Lai, "Prediction of natural frequencies of finite length circular cylindrical shells," Appl. Acoust. **59**(4), 385–400 (2000).
- <sup>37</sup>P. Witczak, "Analytical approach calculating eigenfrequencies and modes of stator cores in AC machines," Arch. Electr. Eng. 61, 47–56 (2012).
- <sup>38</sup>J. Boisson, F. Louf, J. Ojeda, X. Mininger, and M. Gabsi, "Analytical approach for mechanical resonance frequencies of high-speed machines," IEEE Trans. Ind. Electron. **61**(6), 3081–3088 (2014).
- <sup>39</sup>M. Heckl, "Schallabstrahlung von punktförmig angeregten Hohlzylindern" ("Sound radiation from point-excited hollow cylinders"), Acustica 9(371), 86-92 (1959).
- <sup>40</sup>N. Osztovits and S. Hakansson, "Analysing the effects of integration on the noise from electric aircraft motors," in Proceedings of the DAGA 2024, Hannover, Germany (March 18-21, 2024).